The Astrophysical Journal, 663:1125–1138, 2007 July 10

GRB 061121: BROADBAND SPECTRAL EVOLUTION THROUGH THE PROMPT AND AFTERGLOW PHASES OF A BRIGHT BURST

K. L. Page,[1] R. Willingale,[1] J. P. Osborne,[1] B. Zhang,[2] O. Godet,[1] F. E. Marshall,[3] A. Melandri,[4] J. P. Norris,[5,6] P. T. O'Brien,[1] V. Pal'shin,[7] E. Rol,[1] P. Romano,[8,9] R. L. C. Starling,[1] P. Schady,[10] S. A. Yost,[11] S. D. Barthelmy,[3] A. P. Beardmore,[1] G. Cusumano,[12] D. N. Burrows,[13] M. De Pasquale,[10] M. Ehle,[14] P. A. Evans,[1] N. Gehrels,[3] M. R. Goad,[1] S. Golenetskii,[7] C. Guidorzi,[8,9] C. Mundell,[4] M. J. Page,[10] G. Ricker,[15] T. Sakamoto,[3] B. E. Schaefer,[16] M. Stamatikos,[3] E. Troja,[1,12] M. Ulanov,[7] F. Yuan,[11] and H. Ziaeepour[9]

Received 2006 December 22; accepted 2007 April 12

ABSTRACT

Swift triggered on a precursor to the main burst of GRB 061121 ($z = 1.314$), allowing observations to be made from the optical to gamma-ray bands. Many other telescopes, including Konus-*Wind*, *XMM-Newton*, ROTSE, and the Faulkes Telescope North, also observed the burst. The gamma-ray, X-ray, and UV/optical emission all showed a peak ~75 s after the trigger, although the optical and X-ray afterglow components also appear early on, before or during the main peak. Spectral evolution was seen throughout the burst, with the prompt emission showing a clear positive correlation between brightness and hardness. The SED of the prompt emission, stretching from 1 eV up to 1 MeV, is very flat, with a peak in the flux density at ~1 keV. The optical to X-ray spectra at this time are better fitted by a broken, rather than single, power law, similar to previous results for X-ray flares. The SED shows spectral hardening as the afterglow evolves with time. This behavior might be a symptom of self-Comptonization, although circumstellar densities similar to those found in the cores of molecular clouds would be required. The afterglow also decays too slowly to be accounted for by the standard models. Although the precursor and main emission show different spectral lags, both are consistent with the lag-luminosity correlation for long bursts. GRB 061121 is the instantaneously brightest long burst yet detected by *Swift*. Using a combination of *Swift* and Konus-*Wind* data, we estimate an isotropic energy of 2.8×10^{53} ergs over 1 keV–10 MeV in the GRB rest frame. A probable jet break is detected at $\sim 2 \times 10^5$ s, leading to an estimate of $\sim 10^{51}$ ergs for the beaming-corrected gamma-ray energy.

Subject headings: gamma rays: bursts — X-rays: individual (GRB 061121)

1. INTRODUCTION

Gamma-ray bursts (GRBs) are intrinsically extremely luminous objects, approaching values of 10^{54} ergs s^{-1} if the radiation is isotropic (e.g., Frail et al. 2001; Bloom et al. 2003). This energy is emitted over all bands in the electromagnetic spectrum; to understand GRBs as fully as possible, panchromatic observations are required over all time frames of the burst.

The *Swift* multiwavelength observatory (Gehrels et al. 2004) is designed to detect and follow up GRBs. With its rapid slewing ability, *Swift* is able to follow bursts and their afterglows from less than a minute after the initial trigger and can often still detect them weeks, and sometimes months, later. On rare occasions, such as when *Swift* triggers on a precursor to the main burst, the prompt emission, as well as the afterglow, can be observed at X-ray and UV/optical wavelengths. GRB 061121, the subject of this paper, is only the third GRB *Swift* has detected in this manner (after GRB 050117 and GRB 060124; Hill et al. 2006 and Romano et al. 2006, respectively), out of the almost 200 bursts triggered on in the first 2 years of the mission.[17] Of these, GRB 061121 is the second well-sampled event (GRB 060124 was the first), and the first for which the UV/Optical Telescope (UVOT) was in event mode.

In addition to the small number of precursor triggers, around 10% of *Swift* bursts show detectable emission over the Burst Alert Telescope (BAT) bandpass by the time the narrow field instruments (NFIs) are on target.

Besides the *Swift* observations of prompt emission, there have been a small number of prompt optical measurements of GRBs, thanks to the increasing number of robotic telescopes around the world. A variety of behaviors have been found, with some optical

[1] Department of Physics and Astronomy, University of Leicester, Leicester LE1 7RH, UK; kpa@star.le.ac.uk.
[2] Department of Physics and Astronomy, University of Nevada, Las Vegas, NV 89154-4002.
[3] NASA Goddard Space Flight Center, Greenbelt, MD 20771.
[4] Astrophysics Research Institute, Liverpool John Moores University, Egerton Wharf, Birkenhead CH41 1LD, UK.
[5] Denver Research Institute, University of Denver, Denver, CO 80208.
[6] Visiting Scholar, Stanford University.
[7] Ioffe Physico-Technical Institute, Laboratory for Experimental Astrophysics, Saint Petersburg 194021, Russian Federation.
[8] Istituto Nazionale di Astrofisica, Osservatorio Astronomico di Brera, I-23807 Merate (LC), Italy.
[9] Dipartimento di Fisica, Universitá di Milano-Bicocca, I-20126 Milano, Italy.
[10] Mullard Space Science Laboratory, University College London, Holmbury St. Mary, Dorking, Surrey RH5 6NT, UK.
[11] University of Michigan, Ann Arbor, MI 48104.
[12] INAF-IASF, Sezione di Palermo, 90146 Palermo, Italy.
[13] Department of Astronomy and Astrophysics, Pennsylvania State University, University Park, PA 16802.
[14] *XMM-Newton* Science Operations Centre, European Space Agency, Villafranca del Castillo, E-28080 Madrid, Spain.
[15] Center for Space Research, Massachusetts Institute of Technology, Cambridge, MA 02139.
[16] Department of Physics and Astronomy, Louisiana State University, Baton Rouge, LA 70803.

[17] GRB 050820A would possibly have also been in this category, but *Swift* entered the South Atlantic Anomaly (SAA) just as a dramatic increase in count rate began (Cenko et al. 2006; Page et al. 2005a, 2005b; Cummings et al. 2005; Chester et al. 2005); *Swift* does not actively collect data during SAA passages.

(and infrared) light curves tracking the gamma-ray emission (e.g., GRB 041219A; Vestrand et al. 2005; Blake et al. 2005), while others appear uncorrelated (e.g., GRB 990123, Akerlof et al. 1999; Panaitescu & Kumar 2007; although see also Tang & Zhang 2006; GRB 050904, Boër et al. 2006; GRB 060111B, Klotz et al. 2006; GRB 060124, Romano et al. 2006). GRB 050820A (Vestrand et al. 2006) showed a mixture of both correlated and uncorrelated optical flux.

Where correlations exist between different energy bands, it is likely that there is a common origin for the components. In the uncorrelated cases, the optical emission may be due to an external reverse shock (e.g., Sari & Piran 1999; Mészáros & Rees 1999), while the prompt gamma rays are caused by internal shocks. Cenko et al. (2006) suggest that the early optical data for GRB 050820A are produced by the forward shock passing through the band. In the case of GRB 990123, Panaitescu & Kumar (2007) have suggested that the gamma rays arose from inverse Comptonization, while the optical emission was due to synchrotron processes; they do not assume a specific mechanism for the energy dissipation, allowing for the possibility of either internal or reverse-external shocks.

It is unclear whether precursors are ubiquitous features of GRBs, often remaining undetected because of a low signal-to-noise ratio or being outside the energy bandpass of the detector, or whether only some bursts exhibit them. A detailed discussion of the precursor phenomenon is beyond the scope of this paper and will be addressed in a future publication.

In this paper we report on the multiwavelength observations of both the prompt and afterglow emission of GRB 061121. Section 2 details the observations made by *Swift*, Konus-*Wind*, *XMM-Newton*, ROTSE (Robotic Optical Transient Search Experiment), and the Faulkes Telescope North (FTN), with multiband comparisons being made. In § 3, we discuss the precursor, prompt, and afterglow emission, with a summary given in § 4.

Throughout the paper, the main burst (∼60–200 s after the trigger) will be referred to as the prompt emission, and the emission seen over −5 to +10 s as the precursor, where the BAT trigger time $T_0 = 0$ s. Errors are given at 90% confidence (e.g., $\Delta\chi^2 = 2.7$ for one interesting parameter) unless otherwise stated, and the convention $F_{\nu,t} \propto \nu^{-\beta} t^{-\alpha}$ (with the photon spectral index $\Gamma = \beta + 1$ where $dN/dE \propto E^{-\Gamma}$) has been followed. We have assumed a flat universe, with Hubble constant $H_0 = 70$ km s^{-1} Mpc^{-1}, cosmological constant $\Omega_\Lambda = 0.73$, and $\Omega_{\rm matter} = 1 - \Omega_\Lambda$.

2. OBSERVATIONS AND ANALYSES

Two years and one day after launch, the BAT (Barthelmy et al. 2005) triggered on a precursor to GRB 061121 at 15:22:29 UT on 2006 November 21 (Page et al. 2006b). *Swift* slewed immediately, resulting in the NFIs being on target and beginning to collect data 55 s (X-Ray Telescope [XRT]; Burrows et al. 2005b) and 62 s (UVOT; Roming et al. 2005) later. This enabled broadband observations of the main burst event, which peaked ∼75 s after the trigger, leading to spectacular multiwavelength coverage of the prompt emission. The most accurate *Swift* position for this burst was that determined by the UVOT: R.A. = $09^{\rm h}48^{\rm m}54.55^{\rm s}$, decl. = $-13^\circ 11' 42.4''$ (J2000.0; 90% confidence radius of $0.6''$; Marshall et al. 2006); the refined XRT position is only $0.1''$ from these coordinates (Page et al. 2006a).

GRB 061121 was declared a "burst of interest" by the *Swift* team (Gehrels et al. 2006a), to encourage an intensive ground- and space-based follow-up program. In addition to the *Swift* observations, the prompt emission of GRB 061121 was detected by *RHESSI* (Bellm et al. 2006), Konus-*Wind*, and Konus-A (Golenetskii et al. 2006). Later afterglow observations were obtained in the X-ray (*XMM-Newton*; Schartel 2006) and radio (Very Large Array [VLA];[18] Chandra & Frail 2006) bands. The Australia Telescope Compact Array (ATCA) and Westerbork Synthesis Radio Telescope (WSRT) also observed in the radio band between ∼5.2 and ∼6.2 days after the burst but did not detect the afterglow (van der Horst et al. 2006a, 2006b), implying that it had faded since the VLA observation.

Likewise, extensive optical follow-up observations were performed: ROTSE-IIIa (Yost et al. 2006), FTN (Melandri et al. 2006), Kanata 1.5 m telescope (Uemura et al. 2006), the University of Miyazaki 30 cm telescope (Sonoda et al. 2006), Michigan-Dartmouth-MIT Observatory (MDM; Halpern et al. 2006a, 2006b; Halpern & Armstrong 2006a, 2006b), Palomar 60 inch (P60; Cenko 2006), Automated Response Telescope (ART; Torii 2006), the Crimean Astrophysical Observatory (CrAO) 2.6 m telescope (Efimov et al. 2006a, 2006b), and SMARTS/ANDICAM (Small and Moderate Aperture Research Telescope System/A Novel Double-Imaging CAMera; at infrared wavelengths, too; Cobb 2006) all detected the optical afterglow. Spectroscopic observations were performed at the Keck telescope about 12 minutes after the trigger, finding a redshift of $z = 1.314$ for the optical afterglow, based on absorption features (Perley & Bloom 2006; Bloom et al. 2006).

GRB 061121 has the highest instantaneous peak flux of all the long bursts detected by *Swift* to date (e.g., L. Angelini et al. 2007, in preparation).

2.1. *Gamma-Ray Data*

2.1.1. *BAT*

2.1.1.1. Temporal Analysis

After the initial precursor, the BAT count rate returned to close to the instrumental background level, until $T_0 + 60$ s, at which point the much brighter main burst began. This is characterized by a series of overlapping peaks, each brighter than the previous one, after which the gamma-ray flux decayed (from $\sim T_0 + 75$ s to $\sim T_0 + 140$ s). Event data were collected until almost 1 ks after the trigger, thus covering the entire emission period.

T_{90}, over 15–150 keV, and incorporating both the precursor and main emission, is 81 ± 5 s, measured from 8.8 to 89.8 s after the trigger.[19] Figure 1 shows the mask-weighted BAT light curve in the four standard energy bands [15–25 keV, 25–50 keV, 50–100 keV, 100–150 keV; 64 ms binning between 50 and 80 s after the trigger, with 1 s bins at all other times; units of counts s^{-1} (fully illuminated detector)$^{-1}$], with light curves from other instruments: the precursor and the pulses of the main burst are detected over all gamma-ray bands, although the precursor is only marginal over the 100–150 keV BAT band. There is also a soft tail (detected below ∼50 keV, when sufficiently coarse time bins are used) visible until about 140 s after the trigger (see bottom panel of Fig. 1), corresponding to a similar feature in the X-ray light curves.

2.1.1.2. Spectral Analysis

For the precursor, $T_{90,\rm pre} = 7.7 \pm 0.5$ s (15–150 keV). A spectrum extracted over this interval can be well modeled by a single power law, with $\Gamma = 1.68 \pm 0.09$ (χ^2/dof = 26.2/23); no significant improvement was found by using the Band function

[18] The National Radio Astronomy Observatory is a facility of the National Science Foundation operated under cooperative agreement by Associated Universities, Inc.

[19] Errors on the BAT T_{90} are estimated to be typically 5%–10%, depending on the shape of the light curve.

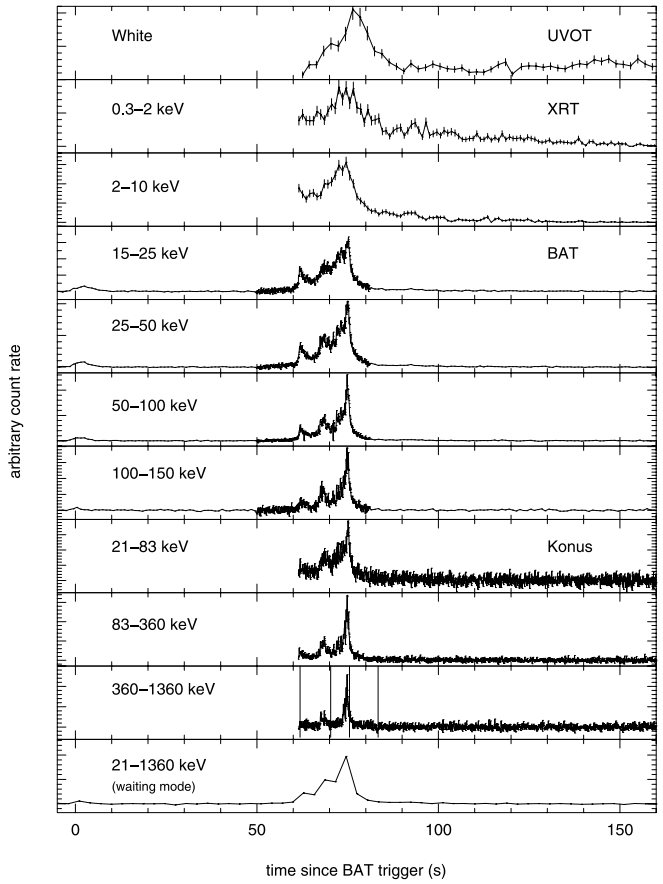

FIG. 1.—*Top panels*: *Swift* UVOT, XRT, BAT, and Konus-*Wind* light curves of GRB 061121; 1 σ error bars are shown for the UVOT and XRT data. Each instrument detected the peak of the main burst, with the precursor being detected over all gamma-ray energies. The vertical lines in the 360–1360 keV panel indicate the start and stop times for the spectra given in Table 1. *Bottom panel*: The 15–50 keV BAT light curve, with 10 s bins, showing a tail out to ~140 s.

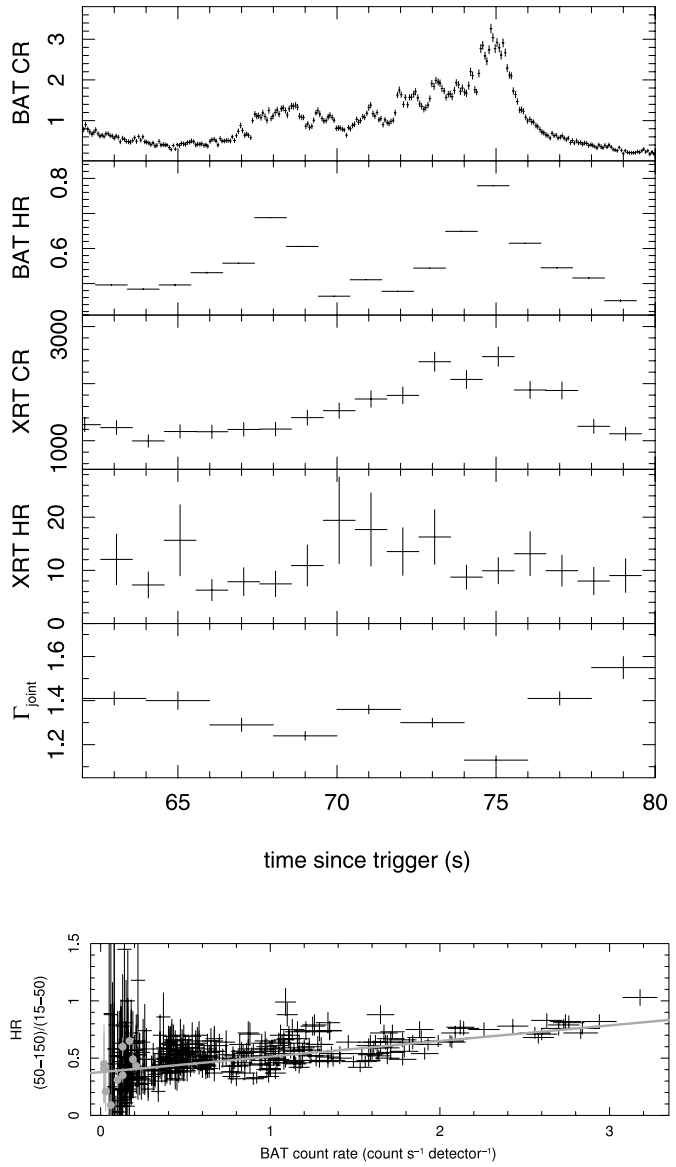

FIG. 2.—*Top panels*: Light curves, hardness ratios (HR), and the variation in Γ using a single power-law fit during the main emission. The BAT light curve (*top panel*) is in units of counts s^{-1} (fully illuminated detector)$^{-1}$, and the corresponding hardness ratio plots (50–150 keV)/(15–50 keV) using 1 s binning. The XRT light curve shows counts over 0.3–10 keV, while the hardness ratio compares (1–10 keV)/(0.3–1 keV) over 1 s bins. *Bottom panel*: BAT hardness ratio vs. count rate, showing that the emission is harder when brighter. Data from the precursor are shown as gray circles, with the main burst in black. The gray line shows a fit to the data, of the form HR = 0.14CR + 0.39.

(Band et al. 1993) or a cutoff power law, and a thermal model led to a slightly ($\chi^2 \sim 8$) worse fit. The 15–150 keV fluence for this time interval is 4×10^{-7} ergs cm^{-2}.

Considering only the main event, $T_{90,\,\mathrm{main}} = 18.2 \pm 1.1$ s (measured from 61.8 to 80.0 s posttrigger). Fitting a power law to the mean spectrum during this time also results in a good fit ($\Gamma = 1.40 \pm 0.01$; fluence $= 1.31 \times 10^{-5}$ ergs cm^{-2} over 15–150 keV; χ^2/dof $= 51.6/56$); again, neither the Band function nor a cutoff power law improves on this. There is significant spectral evolution during the T_{90} period, as shown in Figure 2: at times when the count rate is higher, the spectrum is harder. This behavior was also common in earlier bursts, as well as previous *Swift* detections (e.g., Golenetskii et al. 1983; Ford et al. 1995; Borgonovo & Ryde 2001; Goad et al. 2007). The precursor shows a similar dependence of hardness ratio on count rate, suggesting that the emission processes in the precursor and the main burst are the same or similar.

2.1.2. *Konus-Wind*

2.1.2.1. Temporal Analysis

Konus-*Wind* (Aptekar et al. 1995) triggered on the main episode of GRB 061121, while Konus-A triggered on the precursor (Golenetskii et al. 2006). Because of the spatial separation of *Swift* and *Wind*, the light-travel time between the spacecraft is 1.562 s: the Konus-*Wind* trigger time is $T_{0,\,\mathrm{K}\text{-}W} = T_{0,\,\mathrm{BAT}} + 61.876$ s. All Konus light curves have been plotted with respect to the BAT trigger, corrected for the light-travel time. Figure 1 shows the Konus-*Wind* data plotted over the standard energy bands, with 64 ms binning; the bottom panel plots the coarser time resolution (2.944 s) "waiting mode" data, showing that Konus-*Wind* did see slightly enhanced emission at the time of the precursor. The background levels (which have been subtracted

TABLE 1
KONUS-*Wind* CUTOFF POWER-LAW SPECTRAL FIT RESULTS

Start Time (s)	Stop Time (s)	Γ	E_{peak} (keV)	Γ_{Band}	χ^2/dof
61.876.....	70.324	$1.40^{+0.08}_{-0.09}$	478^{+158}_{-99}	<2.1	72/75
70.324.....	75.188	$1.23^{+0.05}_{-0.06}$	608^{+87}_{-71}	<2.9	88/75
75.188.....	83.380	$1.30^{+0.11}_{-0.13}$	621^{+282}_{-159}	<2.3	81/75
61.876.....	83.380	$1.32^{+0.04}_{-0.05}$	606^{+90}_{-72}	<2.7	95/75

NOTES.—Times are given with respect to the BAT trigger. Γ_{Band} is the upper limit obtained for the spectral index above E_{peak} when fitting with the Band function.

in each case) were 1005, 370, and 193.4 counts s^{-1} for bands 21–83 keV, 83–360 keV, and 360–1360 keV, respectively.

2.1.2.2. Spectral Analysis

Table 1 gives the spectral fits to the Konus-*Wind* data in three separate time intervals shown by vertical lines in Figure 1 (Konus-*Wind* spectral intervals are automatically selected on board): up to the end of the "bump" around 70 s (the "start" of the burst), the burst maximum, and, finally, until most of the emission has died away (the burst tail). The data were fitted with a cutoff power law, where $dN/dE \sim E^{-\Gamma} e^{-(2-\Gamma)E/E_{peak}}$, leading to the photon indices and peak energies given in the table. The Band function was used to estimate upper limits for the photon index above the peak; the values for the peak energy and Γ obtained from the Band function were the same as when fitting the cutoff power law. Little variation in the spectral slope for energies below the peak is seen over these intervals, although the peak itself may have moved to somewhat higher energies during the burst emission. Extracting BAT spectra over the same time intervals and fitting with the same model (fixing E_{peak} at the value determined from the Konus-*Wind* data) results in consistent spectral indices.

2.2. *X-Ray Data*

2.2.1. *XRT*

2.2.1.1. Temporal Analysis

The XRT identified and centroided on an uncataloged X-ray source in a 2.5 s Image Mode (IM) frame, as soon as the instrument was on target. This was quickly followed by a pseudo Piled-up Photo Diode (PuPD) mode frame. Following damage from a micrometeoroid impact in 2005 May (Abbey et al. 2005), the Photo Diode mode (Low Rate and Piled-up) has been disabled (for details on the different XRT modes see Hill et al. 2004); however, the XRT team is currently working on a method to reimplement these science modes and to update the ground software to process the files. The pseudo PuPD point presented here is the first use of such data.

Data were then collected in Windowed Timing (WT) mode starting at a count rate of ~1280 counts s^{-1} (pileup corrected; see below); the rate rapidly increased to a maximum of ~2500 counts s^{-1} at $T_0 + 75$ s, making GRB 061121 the brightest burst yet detected by the XRT. Following this peak, the count rate decreased, with a number of small flares superimposed on the underlying decay (see Fig. 1). Photon Counting (PC) mode was automatically selected when the count rate was below about 10 counts s^{-1}. Around 1.5 ks, the XRT switched back into WT mode briefly, due to an enhanced background linked to the sunlit Earth and a relatively high CCD temperature.

Because of the high count rate, the early WT data were heavily piled up; see Romano et al. (2006) for information about pileup in this mode. To account for this, an extraction region was used

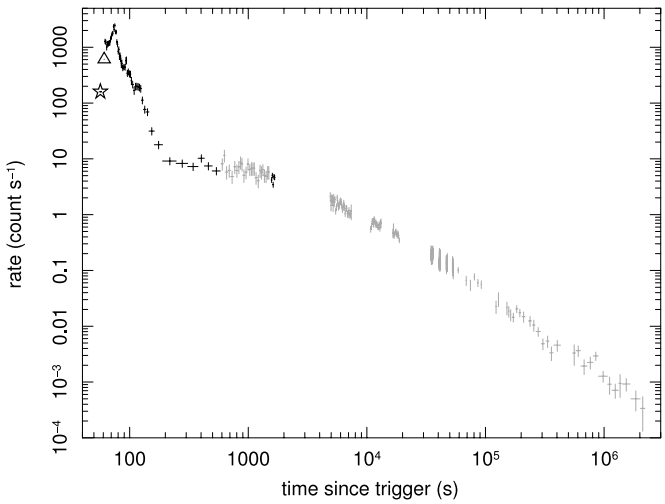

FIG. 3.—*Swift* XRT light curve of GRB 061121. The star and triangle show the initial Image Mode and pseudo-PuPD point (see text for details), followed by WT mode data (*black*) during the main burst (and at the end of the first orbit) and PC mode data (*gray*).

that excluded the central 20 pixels (diameter; 1 pixel = 2.36″) and extended out to a total width of 60 pixels. Likewise, the first three orbits of PC data were piled up, and the data were thus extracted using annular regions (inner exclusion diameter decreasing from 12 to 6 to 4 pixels as the afterglow faded; outer diameter 60 pixels). The count rate was then corrected for the excluded photons by a comparison of the ancillary response files (ARFs) generated with and without a correction for the point-spread function (PSF); the ratio of these files provides an estimate of the correction factor. Nousek et al. (2006) give more details on this method. Occasionally, the afterglow was partially positioned over the CCD columns disabled by micrometeoroid damage mentioned above. In these cases, the data were corrected using an exposure map.

From $T_0 + 3 \times 10^5$ s onward, the afterglow had faded sufficiently for a nearby (41.5″ away), constant (count rate ~0.003 counts s^{-1}) source to contaminate the GRB region; this source is coincident with a faint object in the Digitized Sky Survey and is marginally detected in the UVOT *V* filter. Thus, beyond this time, the extraction region was decreased to a diameter of 30 pixels, and the count rates corrected for the loss in PSF (a factor of ~1.08). The spectrum of this nearby source can be modeled with a single power law of $\Gamma = 1.5^{+0.2}_{-0.1}$, with $N_H = (1.8^{+1.6}_{-1.2}) \times 10^{21}$ cm^{-2}, in comparison with the Galactic value in this direction of 5.09×10^{20} cm^{-2} (Dickey & Lockman 1990).

Figure 3 shows the XRT light curve, starting with the IM point (for details on how IM data are converted to a count rate see Hill et al. 2006) and followed by the pseudo-PuPD mode data. The importance of these early pre-WT data is clear, confirming that the XRT caught the rise of the main burst.

After the bright burst, the afterglow began to follow the "canonical" decay, seen in many *Swift* bursts (Nousek et al. 2006; Zhang et al. 2006). Such a decay can be parameterized by a series of power-law segments; in this case, fitting the data beyond 200 s after the trigger (=125 s after the main peak), two breaks in the light curve were identified, with the decay starting off very flat ($\alpha = 0.38 \pm 0.08$) and eventually steepening to $\alpha = 1.07^{+0.04}_{-0.06}$ at ~2.3 ks and then $\alpha = 1.53^{+0.09}_{-0.04}$ at ~32 ks (Table 2). The addition of the second break vastly improved the fit by $\Delta\chi^2 = 112.4$ for 2 degrees of freedom. However, we note that O'Brien et al. (2006) and Willingale et al. (2007) advocate a

TABLE 2
XRT Power-Law Light-Curve Fits

Parameter	Value	Epoch
α_1	0.38 ± 0.08	Plateau phase
$T_{\rm break,1}$ (s)	2258^{+507}_{-377}	Plateau phase
α_2	$1.07^{+0.04}_{-0.06}$	Shallow phase
$T_{\rm break,2}$ (s).....	$(3.2^{+2.1}_{-0.6}) \times 10^4$	Shallow phase
α_3	$1.53^{+0.09}_{-0.04}$	Steep phase

Notes.—XRT power-law light-curve fits from 200 s after the trigger onward; times are referenced to the BAT trigger. The names used in the text for the different epochs of the light curve are listed in the last column.

different description of the temporal decline; we return to this in § 3.

Fitting the decay of the main peak (75–200 s, keeping T_0 as the trigger time) with a power law, the slope is very steep, with $\alpha_0 = 5.1 \pm 0.2$. However, both Zhang et al. (2006) and Liang et al. (2006) have shown that the appropriate time origin is the start of the last pulse. Thus, a model of the form $f(t) \propto (t - t_0)^{-\alpha_0}$ was used, finding $t_0 = 58 \pm 1$ s and a slope of $\alpha_0 = 2.2^{+0.4}_{-0.3}$; this is a statistically significant improvement on the power-law fit using the precursor T_0 ($\Delta\chi^2 = 32$ for one extra parameter).

Figure 4 plots the *Swift* data in terms of flux (the BAT data have been extrapolated into the 0.3–10 keV band, using the joint fits with the XRT described in § 2.4.1) and flux density for UVOT. The BAT and XRT data are fully consistent with each other at all overlapping times.

2.2.1.2. Spectral Analysis

The XRT data also show that strong spectral evolution was present throughout the period of the prompt emission; this is discussed in conjunction with the BAT data in § 2.4.1. Considering the X-ray data alone, there is some indication that the spectra may be better modeled with a broken, rather than single, power law, although the break energies cannot always be well constrained (see Fig. 5). For each spectrum (covering periods of 2 s during the main pulse, followed by two spectra of 5 s [80–85 s and 85–90 s] where the emission is fainter), the low-energy

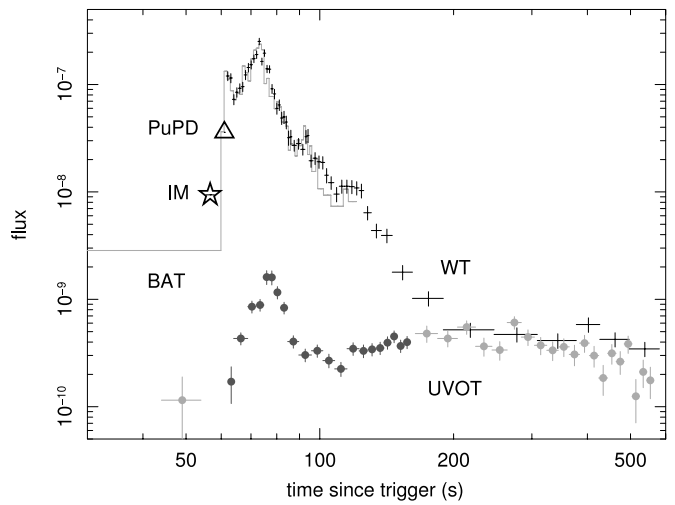

Fig. 4.—*Swift* flux light curve of GRB 061121, showing the early X-ray data (*star, triangle, and crosses*) and the BAT data (*gray histogram*) extrapolated into the 0.3–10 keV bandpass in units of ergs cm^{-2} s^{-1}, together with the UVOT flux density light curve (*light gray circles*: *V* band; *dark gray circles*: White filter) in units of ergs cm^{-2} s^{-1} Å^{-1}, scaled to match the XRT flux observed at the start of the plateau phase.

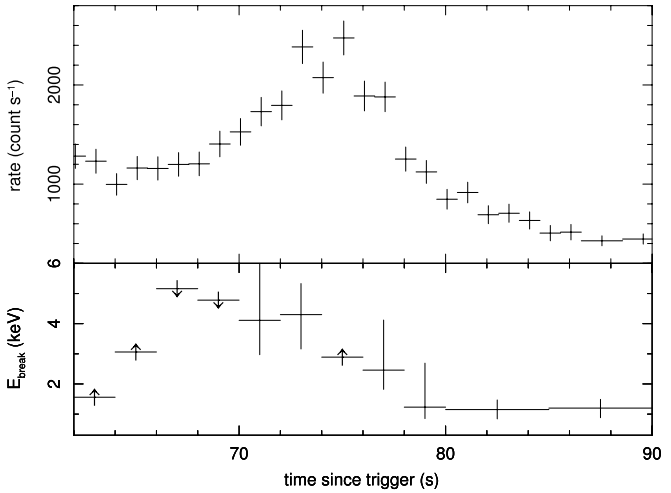

Fig. 5.—Fitting the X-ray data over 0.3–10 keV with a broken power law ($\Gamma_1 = 0.69^{+0.13}_{-0.07}$ and $\Gamma_2 = 1.61^{+0.14}_{-0.13}$ for all spectra), the break energy seems to move through the band, toward higher energies when the emission is brighter. Arrows indicate upper or lower 90% limits.

slopes were tied together for each spectrum (i.e., the slope measured is that averaged over all of the spectra), as were the high-energy indices, and the rest-frame column density, $N_{{\rm H},z}$, was fixed at $(9.2 \pm 1.2) \times 10^{21}$ cm^{-2} from the best fit to the data from later times (see below); only the break energy and the normalization were allowed to vary. When simultaneously fitting all 11 spectra, χ^2/dof decreased from 142/134 to 127/132. Individually, the spectral fits were typically improved by χ^2 of between 2 and 5.

The X-ray data during the GRB 051117A flares (Goad et al. 2007) were found to be better modeled with broken power laws, with the break energy moving to harder energies during each flare rise, and then softening again as the flux decayed. Likewise, Guetta et al. (2007) found breaks in the X-ray spectra obtained during the flares in GRB 050713A. The same pattern may be occurring here, and there is certainly an indication of spectral curvature.

The observed flux calculated from the spectrum corresponding to the peak of the emission (74–76 s) was measured to be 1.66×10^{-7} ergs cm^{-2} s^{-1} (over 0.3–10 keV); the unabsorbed value was 1.77×10^{-7} ergs cm^{-2} s^{-1}.

The PC spectra were also extracted for the various phases of the light curve ("plateau," "shallow," and "steep;" defined in Table 2); the results of the fitting are presented in Table 3. In each phase, the spectrum could be well modeled by a single power law (no break required), with excess absorption in the rest frame of the GRB (modeled using ZTBABS and the "Wilms" abundance in XSPEC; Wilms et al. 2000). Together with the WT spectrum from ~200 to 590 s after the trigger (in the plateau stage), the first two PC spectra (plateau and shallow) are fully consistent with a constant photon index of $\Gamma = 2.07 \pm 0.06$ and $N_{{\rm H},z} = (9.2 \pm 1.2) \times 10^{21}$ cm^{-2}.

Following the second apparent break in the light curve, around 3.2×10^4 s, the spectrum hardened slightly, to a photon index of $\Gamma = 1.83 \pm 0.11$ (or 1.87 ± 0.08 using $N_{{\rm H},z} = 9.2 \times 10^{21}$ cm^{-2}).

2.2.2. *XMM-Newton*

XMM-Newton (Jansen et al. 2001) performed a Target of Opportunity observation of GRB 061121 (observation ID 0311792101) less than 6.5 hr after the trigger (Schartel 2006) and collected data for ~38 ks (MOS1, MOS2; Turner et al. 2001) and ~35 ks (pn; Strüder et al. 2001). This observation is mainly during the

TABLE 3
XRT PC Spectral Fits

Γ	$N_{H,z}$ (10^{21} cm^{-2})	χ^2/ν	Corresponding α	Epoch	Time Since Trigger (s)
2.14 ± 0.12.....	$10.8^{+2.5}_{-2.8}$	62.5/52	0.38 ± 0.08	Plateau	590–1560
2.04 ± 0.10.....	$8.9^{+2.1}_{-2.4}$	67.5/70	$1.07^{+0.04}_{-0.06}$	Shallow	4900–22245
1.83 ± 0.11.....	$8.0^{+2.6}_{-2.2}$	48.0/55	$1.53^{+0.09}_{-0.04}$	Steep	34550–1152750
2.09 ± 0.08.....	9.2 ± 1.2 (tied)	63.5/53	0.38 ± 0.08	Plateau	590–1560
2.05 ± 0.06.....	9.2 (tied)	67.6/71	$1.07^{+0.04}_{-0.06}$	Shallow	4900–22245
1.87 ± 0.08.....	9.2 (tied)	48.7/56	$1.53^{+0.09}_{-0.04}$	Steep	34550–1152750

Notes.—XRT PC spectral fits, with rest-frame N_H free and then tied between all three spectra. The temporal decay slopes, α, corresponding to each stage are also given. The Galactic absorbing column of $N_H = 5.09 \times 10^{20}$ cm^{-2} was always included in the model.

shallow phase, although it also covers a short time span after the break at around 32 ks.

Figure 6 plots the pn flux light curve and hardness ratio during the *XMM-Newton* observation, showing the lack of spectral evolution during this time frame; a hardness ratio calculated for the *Swift* data was in agreement with this finding. The decay slope over this time (MOS1, MOS2, pn, and joint) is consistent with the *Swift* results ($\alpha \sim 1.3$; note that this crosses the time of the second break in the decay).

The *XMM-Newton* European Photon Imaging Camera (EPIC) spectra show clear evidence for excess N_H, in agreement with the *Swift* data. In addition, fitting with excess N_H in the rest frame of the GRB gives a significantly better fit than at $z = 0$, as shown in Figure 7. When fitting in the observer's frame, there is a noticeable bump in the residuals around 0.6 keV; fitting with N_H at $z = 1.314$ removes this feature. The data are of sufficiently high signal-to-noise ratio that the redshift of the absorber can be estimated from the spectrum. Limits can be placed on the redshift and absorbing column, respectively, of $z > 1.2$ and $N_{H,z} > 4.6 \times 10^{21}$ cm^{-2} at 99% confidence, in agreement with the spectroscopic redshift from Bloom et al. (2006) within the statistical uncertainties. At their value of $z = 1.314$, the excess $N_{H,z}$ from the EPIC pn spectrum is $(5.3 \pm 0.2) \times 10^{21}$ cm^{-2}, lower than the best fit to the *Swift* data from the simultaneous shallow decay section, but more similar to the values obtained from fitting the optical to X-ray spectral energy distributions (SEDs) in § 2.4.2. In agreement with the simultaneous XRT PC mode data, there is no evidence for a break in the EPIC spectrum over this time period. Spectra from neither the Reflection Grating Spectrometer (den Herder et al. 2001) nor EPIC show obvious absorption or emission lines.

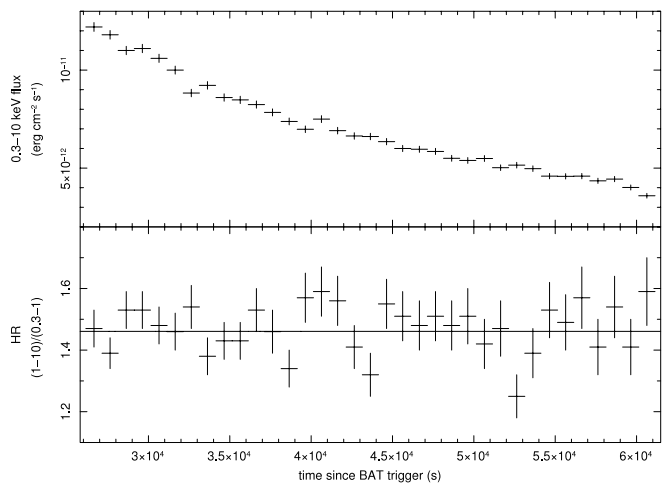

Fig. 6.—*XMM-Newton* EPIC pn light curve and hardness ratio of GRB 061121. The horizontal line shows that the hardness ratio is consistent with a constant value of ~1.46, indicating that there is no spectral evolution during this time.

2.2.3. *Chandra*

Chandra performed a 33 ks Target of Opportunity observation at ~61 days after the trigger. No source was detected at the position of the X-ray afterglow, with a 3 σ upper limit of 2.5×10^{-15} ergs cm^{-2} s^{-1}.

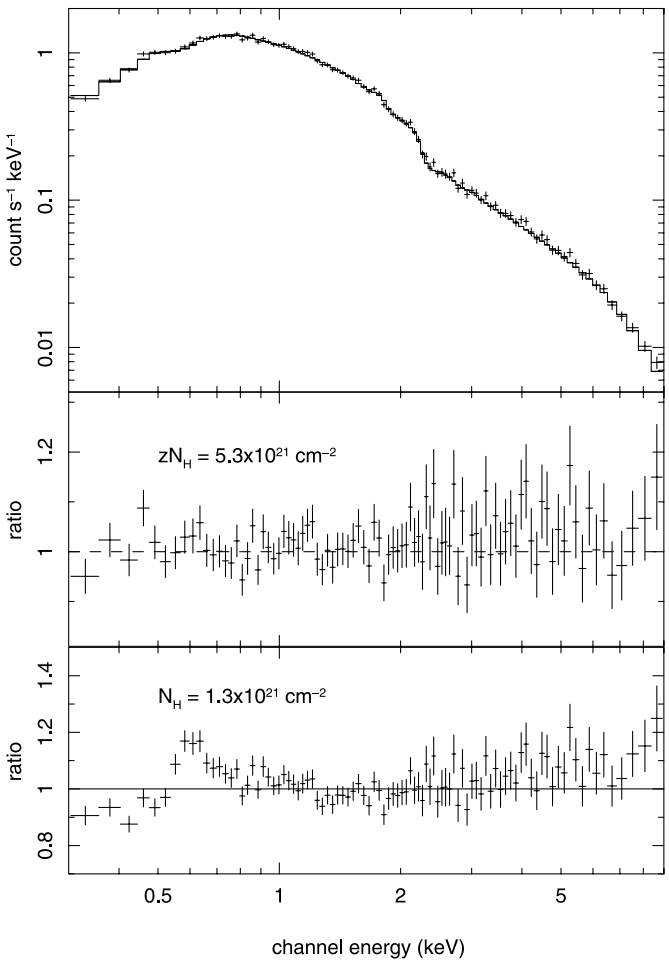

Fig. 7.—EPIC pn spectrum of the late-time afterglow of GRB 061121, with an excess absorbing column in both the rest frame of the GRB and the observer's frame. The spectrum is much better modeled with an excess column at $z = 1.314$.

modify the afterglow (Zhang et al. 2006); the later two stages both have $q > 1$. However, as discussed in § 3.3.2, the plateau and final transition to the power-law decay are only visible in the X-ray data for GRB 061121; the start of the final decay is much earlier in the *V* and *R* bands (see Fig. 10). One might expect that energy injection would affect all the energy bands simultaneously, rather than just the X-rays.

From the standard afterglow model computations (e.g., Zhang & Mészáros 2004), we find that none of the closure relations fit the entire data set completely: although the shallow phase (after the end of energy injection, between $T + 2.3$ ks and $T + 32$ ks) could be consistent with the evolution of a blast wave that had already entered the slow-cooling regime when deceleration started [i.e., $\nu > \max(\nu_m, \nu_c)$, where ν_c is the cooling frequency and ν_m is the synchrotron injection frequency; Sari et al. 1998; Chevalier & Li 2000], the steeper part of the decay curve ($T > 32$ ks) is not consistent with any of the models. This lack of consistency suggests that a different approach is required.

The change in decay slope between the shallow to steep phases ($\sim$32 ks) cannot be easily identified with a jet break. It certainly seems unlikely that the simplest side-spreading jet model could be applicable, since the postbreak decay index ($\alpha \sim 1.5$) is not steep enough (a postjet decay has $\alpha = p$, where p is the electron index). There is also some indication that the X-ray spectral slope hardens after the break, whereas no change in spectral signature is expected over a jet break. In the case of a nonlaterally expanding jet (Panaitescu & Mészáros 1999), $\alpha = (3\beta/2) + 0.25$ (for a homogeneous circumstellar medium [CSM]; Panaitescu et al. 2006b), which does, indeed, fit the data after this break: $[1.5 \times (0.9 \pm 0.08)] + 0.25 = 1.6 \pm 0.1$; the measured α is 1.53. Such a confined jet has been suggested as an explanation for the observed decay in a number of previous bursts (e.g., GRB 990123, Kulkarni et al. 1999; GRB 050525A, Blustin et al. 2006; GRB 061007, Schady et al. 2006). The UVOT data obtained around this time show little evidence for a break, whereas jet breaks should occur across all energy bands simultaneously. However, nonsimultaneity could be explained by a multicomponent outflow, where the X-ray emission is produced within a narrow jet, while the optical component comes from a wider jet with lower Lorentz factor (Panaitescu & Kumar 2004; Oates et al. 2007). There remains the issue, however, that α should steepen by 0.75 over a jet break (Mészáros & Rees 1999), whereas the maximum observed change (within the 90% errors) is only $\Delta\alpha < 0.61$, excluding $\Delta\alpha = 0.75$ at almost 3 σ; also, again there should be no spectral evolution across the break. There is, however, a probable jet break at later times, which is covered in the next section.

Other multicomponent models (see, e.g., Oates et al. 2007 and references therein) also fail to explain the data because of the lack of observed energy injection (plateau phase) in the optical data.

Panaitescu et al. (2006a) discuss chromatic breaks in *Swift* light curves and postulate that these could be due to a change in microphysical parameters within a wind environment. However, this model requires the cooling frequency to lie between the X-ray and optical bands and, as is discussed in § 3.3.2, this does not seem to be the case here.

3.3.2. *Exponential to Power-Law Decline Model*

As first described by O'Brien et al. (2006) and further expanded by Willingale et al. (2007), GRB light curves can be well modeled by one or two components comprised of an early exponential rise followed by a power-law decay phase. Of these components, the first represents the prompt gamma-ray emission and early X-ray decay. The second, when detected, dominates at later times, forming what we see as the afterglow. These results show that fitting an intrinsically curved decay with multiple power-law segments runs the risk of incorrectly identifying temporal breaks (see also T. Sakamoto et al. 2007, in preparation). In this section the models of O'Brien et al. (2006) and Willingale et al. (2007) are applied to the multiband afterglow data of GRB 061121.

Figure 10 brings together the BAT, XRT, UVOT, FTN, and ROTSE data, along with further optical and radio points taken from the GCN Circulars (Halpern et al. 2006a, 2006b; Halpern & Armstrong 2006a, 2006b; Chandra & Frail 2006; van der Horst et al. 2006a, 2006b) and the upper limit from *Chandra*, to form a multienergy decay plot. The data have been plotted as "time since trigger + 4 s" in order to include the precursor on a log timescale. The optical points have all been corrected for extinction using $A_V = 1.2$ (a combination of the Galactic value of 0.151 and an estimate of $A_V \sim 1$ for the GRB host galaxy; see § 2.4.2).

The contribution from the host galaxy reported by Malesani et al. (2006) and Cobb (2006) has been subtracted from the *V*- and *R*-band flux values. The magnitude of the host in the *V* band is 22.4, which only changes the last two or three *V*-band points by a small amount. For the *R* band we have no direct measurement, but the last group of MDM exposures gave an *R* magnitude of 22.7, corresponding to a flux level of 2.8 μJy, and the flux level is still declining at that epoch ($\sim 3.3 \times 10^5$ s), so an *R*-band flux level of 2.5 μJy was adopted for the host. The error bars shown on the last few points reflect the large uncertainty in the galaxy contribution subtracted.

The curved dotted lines in Figure 10 are the fits to the data using the exponential–to–power-law model, followed by a break to a steeper decay around 10^5 s. These models are parameterized by the power-law decay, α, and T_a, the time at which this decay is established. For the X-ray data, $T_{a,\mathrm{X}}$ is found to be 5250^{+500}_{-460} s and $\alpha_{a,\mathrm{X}} = 1.32 \pm 0.03$. Fits were also performed to the *V*- and *R*-band data, yielding $\alpha_{a,V} = 0.66 \pm 0.04$ (with $T_{a,V} = 70^{+60}_{-70}$ s) and $\alpha_{a,R} = 0.84 \pm 0.03$ ($T_{a,R} = 230^{+120}_{-230}$ s).

The nondetection by *Chandra* almost 2 months after the burst shows that there must have been a further steepening in the X-ray regime, and the optical data are not inconsistent with this finding. Constraining the temporal index after the late break to be $\alpha = 2$ (a typical slope for a post–jet break decay), break times of $\sim 2.5 \times 10^5$, $\sim 2.5 \times 10^4$, and $\sim 10^5$ s are estimated for the X-ray, *V* band, and *R* band, respectively; note that the UVOT *V*-band value is particularly uncertain, given the small number of data points at late times. Within the uncertainties, these times are likely to be consistent, so the turnover could be achromatic, as required for a jet break. From Willingale et al. (2007), a jet break might be expected at $\sim 100 T_{a,\mathrm{X}}$, i.e., 5.5×10^5 s, which is in agreement with these fits.

As can be seen from these numbers and the models plotted in Figure 10, the X-ray data clearly show the transition from the plateau to the power-law decay, whereas the start of the final decay is much earlier in the *V* and *R* bands. The *V*-band decay is also significantly flatter (by $\alpha \sim 0.2$) than that estimated for the *R* band. As previously stated, the *V*, *B*, and *U* light curves are all consistent with this slow decay. There have been few multicolor optical decay curves obtained for GRB afterglows, and, of these, the different filters (in the case of GRB 061007 [Schady et al. 2006; Mundell et al. 2007] X-ray and gamma-ray data, as well as the optical) tend to track each other (e.g., Guidorzi et al. 2005; Blustin et al. 2006; de Ugarte Postigo et al. 2007). In the case of GRB 061121, we find that the *R*-band data are fading more rapidly than the *V*. GRB 060218, which was associated with a supernova (e.g., Campana et al. 2006b), shows changes throughout the optical spectra because of a combination of shock breakout and radioactive heating of the supernova ejecta. There is a large

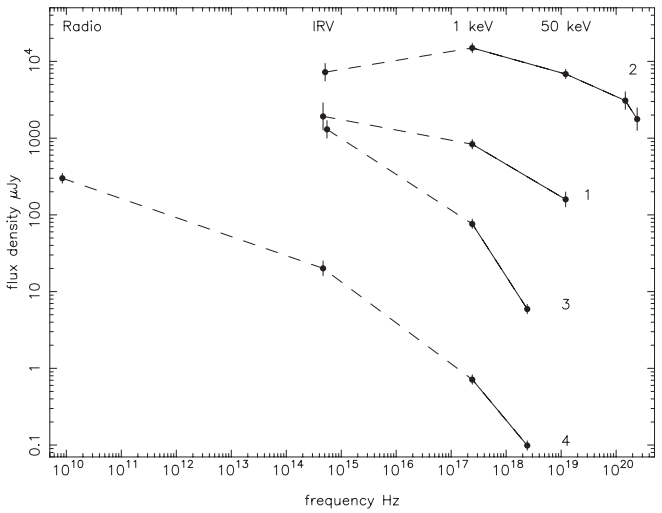

FIG. 11.—SEDs for the four time intervals indicated in Fig. 10. SED 2 (the peak of the burst emission) includes the Konus-*Wind* data, although these have not been included in Fig. 10. The solid lines represent the power-law fits to the BAT, XRT, and Konus data, while the dashed lines join the radio, optical, and 1 keV points. Spectral evolution over time is clearly seen.

difference between the decays of the blue (*V*, *U*, *B*) and red (*R*) data for GRB 061121, which cannot be easily explained by a synchrotron spectrum. Although no supernova has been detected in this case, we speculate that some form of presupernova thermal emission could possibly be affecting the optical data, adding energy into the blue end of the spectrum, thus slowing its decline.

After the break in the decays around 10^5 s, the light curves across all bands become more consistent with one another, although there are only limited data at such a late time.

The vertical dotted lines in Figure 10 show the times of the SEDs plotted in Figure 11; again, all points were corrected for an extinction of $A_V = 1.2$, so that they represent the true SEDs (with the frequency in the observer's frame). The solid lines represent actual fits to the X-ray and gamma-ray data, while the dashed lines just join the separate radio, optical, and 1 keV points. The times of these SEDs, which clearly show spectral evolution, correspond to (1) before the main BAT peak, 56 s after trigger; (2) at the BAT peak, 76 s after trigger; (3) just after the start of the plateau, 300 s after the trigger; and (4) in the main decay at 65 ks (chosen because radio measurements were taken at this time). SEDs 3 and 4 do not contain any BAT or Konus data, since the gamma-ray flux had decayed by this point; the highest energy point in these corresponds to the maximum energy (10 keV) of the X-ray fits.

Table 4 demonstrates that the optical and X-ray spectra during the peak emission are best fitted with a broken power-law model, with the break energy at the very low energy end of the X-ray bandpass. SED 2 in Figure 11 shows that this spectral break corresponds to the peak frequency in a flux density plot (β_1 is less than zero in this case). Only during SED 2 is the optical flux density lower than that of the higher energy data. Figure 4 also shows that the optical emission is less strong than the X-ray and gamma-ray data during the main burst.

Table 5 shows the values of α for the X-ray and optical decays (i.e., before and after the break) in SED 4, at 65 ks, with their corresponding spectral indices. For the initial stages of the power-law decay ($T_a < t < 65{,}000$ s) the evolution of the afterglow SED and the coupling between the temporal and spectral indices are not completely consistent with the standard model: although the *R*-band decay, with $\alpha_{a,R} = 0.84 \pm 0.03$, is in good agreement with the homogeneous CSM model below the cooling break, the X-ray and *V*-band flux decays are slower than expected from the measured spectral indices; they are in best agreement with the same constant density model below ν_c, however.

The point at which the power-law decay dominates the exponential in the optical bands is noticeably earlier than in the X-ray (less than a few hundred seconds, rather than ~5000 s), and, as mentioned above, the decay indices are significantly different for all three (X-ray, *V*, and *R*) bands (see Fig. 10). At the time of SED 3, the X-ray data are not decaying (i.e., this is during the plateau), yet both the *V*- and *R*-band data have already entered the power-law decline phase. The *R* band is decaying faster than the *V* band, so the spectral index through the optical range is becoming harder. The X-ray spectral index shows a similar hardening trend (see Table 3), so the SED measured from optical to 10 keV is gradually getting harder. Such spectral hardening from the plateau to the final decay is a feature of many X-ray afterglows (Willingale et al. 2007).

This slow hardening of the broadband spectrum with time could be a signature of synchrotron self-Compton emission (Sari & Esin 2001; Panaitescu & Kumar 2000). The strength of the self-Compton component in the afterglow depends on the flux of low-energy photons (radio–optical) and the electron density in the shock. Using the formulation in Sari & Esin (2001), the density required is given by

$$n_1 = 3 \times 10^9 \left(\frac{f_{\max}^{\rm IC}}{f_{\max}^{\rm sync}} \right)^{4/3} \left(E_{52} t_{\rm day} \right)^{-1/3} \ {\rm cm}^{-3}, \qquad (1)$$

where $f_{\max}^{\rm IC}/f_{\max}^{\rm sync}$ is the ratio of the peak flux of the seed synchrotron spectrum (i.e., the source of low-energy photons) and the peak flux of the self-Compton emission, E_{52} is the isotropic burst

TABLE 5
CLOSURE RELATIONS

GRB MODELS	$\alpha(\beta)$	$\alpha(\beta_{a,\rm X})$[b]	$\alpha_{a,\rm X}$[a]	$\alpha(\beta_{\rm opt})$[b]	$\alpha_{\rm opt}$[a]	
					V Band	*R* Band
CSM SC[c] ($\nu_m < \nu < \nu_c$)	$3\beta/2$	1.49 ± 0.10	1.32 ± 0.03	0.80 ± 0.09	0.66 ± 0.04	0.84 ± 0.03
Wind SC[c] ($\nu_m < \nu < \nu_c$)	$(3\beta+1)/2$	1.99 ± 0.10	1.32 ± 0.03	1.30 ± 0.09	0.66 ± 0.04	0.84 ± 0.03
CSM or Wind SC[c] and FC[d] [$\nu > \max(\nu_c, \nu_m)$]	$(3\beta-1)/2$	0.99 ± 0.10	1.32 ± 0.03	0.30 ± 0.09	0.66 ± 0.04	0.84 ± 0.03

NOTE.—Closure relations for exponential plus power-law model fits to the X-ray data ($\beta_{a,\rm X} = 0.99 \pm 0.07$) and the optical to X-ray band ($\beta_{\rm opt} = 0.53 \pm 0.06$) from the time of SED 4 (65 ks after the burst).

[a] Observed power-law decay index.
[b] Decay calculated from the measured spectral index.
[c] Slow cooling.
[d] Fast cooling.

energy in units of 10^{52} ergs, and $t_{\rm day}$ is the time in days after the burst (which determines the distance through the CSM swept up by the external shock). From Figure 11 (SEDs 1, 3, and 4) we see that $f_{\rm max}^{\rm IC}/f_{\rm max}^{\rm sync} \sim 0.001$ if the X-ray flux has a significant contribution from a self-Compton component at $t_{\rm day} = 0.75$. A value of $E_{52} = 30$ gives $n_1 \approx 10^5$ cm^{-3}. Even assuming that the emission at 0.75 days is not dominated by the self-Comptonization, and so taking the $f_{\rm max}^{\rm IC}/f_{\rm max}^{\rm sync}$ ratio to be a factor of 10 smaller, the density would be $\sim 5 \times 10^3$ cm^{-3}, which is still high. It seems unlikely that self-Compton emission is the cause of the spectral hardening of the SED unless the CSM density encountered by the external shock is extremely large. However, there have been suggestions that GRBs may form in molecular clouds (Galama & Wijers 2001; Campana et al. 2006a, 2007), which have densities of 10^4 or more particles per cubic centimeter in the cores (Miyazaki & Tsuboi 1999; Wilson et al. 1999). Typically one might expect greater reddening than is found here (Table 4), although Waxman & Draine (2000) discuss the possibility of dust destruction.

The spectrum will be redshifted as the jet slows down, so the optical and X-ray spectral indices should, if anything, become softer, the opposite of what is seen here. Although spectral hardening with time is suggested from the data, it is not easily explained by current models.

Whether or not there is a Comptonized component, the later SEDs clearly indicate that there is a break in the spectrum somewhere between the optical and the X-ray; this is also shown by the fits in Table 4, where the UVOT/XRT spectra are better fitted with broken power laws, with $E_{\rm break}$ toward the low-energy end of the X-ray bandpass. Since both the optical and X-ray bands appear to be below the cooling frequency, from the closure relations given in Table 5, this change in slope cannot be identified with a cooling break; its origin remains unclear.

The redshift of $z = 1.314$ and the isotropic energy of $E_{\rm iso} \sim 3 \times 10^{53}$ ergs (§ 2.4.1) can be used to place constraints on the jet opening angle. From Sari et al. (1999), and assuming that the jet break occurs at $T_0 + 2 \times 10^5$ s, we have $\theta_j \sim 4^\circ (\eta_\gamma/0.2)^{1/8} (n/0.1)^{1/8}$, where n and η_γ are the density of the CSM and the efficiency of the fireball in converting the energy in the ejecta into gamma rays, respectively. Taking $\eta_\gamma = 0.2$ and $n = 3$ cm^{-3} (following Ghirlanda et al. 2004), this gives $E_\gamma \sim 1.7 \times 10^{51}$ ergs for the beaming-corrected gamma-ray energy released, which is within the range previously determined (e.g., Frail et al. 2001) and consistent with the Ghirlanda relationship (Ghirlanda et al. 2004).

4. SUMMARY AND CONCLUSIONS

Swift triggered on a precursor to GRB 061121, leading to unprecedented coverage of the prompt emission by all three instruments on board, with the gamma-ray, X-ray, and optical/UV bands all tracking the main peak of the burst. GRB 061121 is the instantaneously brightest long *Swift* burst detected thus far, in both gamma rays and X-rays. The precursor and main burst show spectral lags of different lengths, although both are consistent with the lag-luminosity relation for long GRBs (Gehrels et al. 2006b).

The SED of the prompt emission, stretching from 1 eV to 1 MeV, shows a peak flux density at around 1 keV and is harder than the standard model predicts. There is definite curvature in the spectra, with the prompt optical to X-ray spectrum being better fitted by a broken power law, similar to results found for fitting X-ray flares (e.g., Guetta et al. 2007; Goad et al. 2007).

The afterglow component, in both the optical and X-ray, starts early on, before or during the main burst peak (see also O'Brien et al. 2006; Willingale et al. 2007; Zhang et al. 2007). The broadband SEDs reveal gradual spectral hardening as the afterglow evolves, both within the X-ray regime (Γ flattening from $\sim$2.05 to $\sim$1.87) and between the *V*- and *R*-band optical data ($\alpha_V \sim 0.66$ compared with $\alpha_R \sim 0.84$). Self-Comptonization could explain the hardening, although a molecular cloud core density would be required. A probable jet break occurs around $T_0 + 2 \times 10^5$ s, shown by a late-time nondetection by *Chandra*. Before this break, the X-ray and *V*-band decays are too slow to be readily explained by the standard models.

This extremely well sampled burst shows clearly that there remains much work to be done in the field of GRB models. A single, unified model for all GRB emission observed should be the ultimate goal.

The authors gratefully acknowledge support for this work at the University of Leicester by PPARC, at PSU by NASA, and in Italy by funding from ASI. This work is partly based on observations with the Konus-*Wind* experiment (supported by the Russian Space Agency contract and RFBR grant 06-02-16070) and on data obtained with *XMM-Newton*, an ESA science mission with instruments and contributions directly funded by ESA Member States and NASA. We thank the Liverpool GRB group at ARI, Liverpool John Moores University, in particular C. J. Mottram, D. Carter, R. J. Smith, and A. Gomboc, for their assistance with the FTN data acquisition and interpretation. The Faulkes Telescopes are operated by the Las Cumbres Observatory Global Telescope Network. We also thank J. E. Hill and A. F. Abbey for discussions and help with the PuPD data, P. Curran for assistance with the UVOT/XRT SED creation, D. Grupe for the *Chandra* upper limit, and B. Cobb and D. Malesani for information regarding the magnitude of the host galaxy. Thanks as well to C. Akerlof, E. Rykoff, A. Phillips, and M. C. B. Ashley from the ROTSE team.

REFERENCES

Abbey, A. F., et al. 2005, in The X-Ray Universe 2005, ed. A. Wilson (ESA-SP 604; Noordwijk: ESA), 943
Akerlof, C., et al. 1999, Nature, 398, 400
Amati, L., et al. 2002, A&A, 390, 81
Aptekar, R. L., et al. 1995, Space Sci. Rev., 71, 265
Band, D., et al. 1993, ApJ, 413, 281
Barthelmy, S. D., et al. 2005, Space Sci. Rev., 120, 143
Bellm, E., Bandstra, M., Boggs, S., Wigger, C., Hajdas, W., Smith, D. M., & Hurley, K. 2006, GCN Circ. 5838, http://gcn.gsfc.nasa.gov/gcn/gcn3/5838.gcn3
Blake, C. H., et al. 2005, Nature, 435, 181
Bloom, J. S., Frail, D. A., & Kulkarni, S. R. 2003, ApJ, 594, 674
Bloom, J. S., Perley, D. A., & Chen, H. W. 2006, GCN Circ. 5826, http://gcn.gsfc.nasa.gov/gcn/gcn3/5826.gcn3
Blustin, A. J., et al. 2006, ApJ, 637, 901
Boër, M., Atteia, J. L., Damerdji, Y., Gendre, B., Klotz, A., & Stratta, G. 2006, ApJ, 638, L71
Borgonovo, L., & Ryde, F. 2001, ApJ, 548, 770
Bouchet, P., Lequeux, J., Maurice, E., Prevot, L., & Prevot-Burnichon, M. L. 1985, A&A, 149, 330
Burrows, D. N., et al. 2005a, Science, 309, 1833
———. 2005b, Space Sci. Rev., 120, 165
Campana, S., et al. 2006a, A&A, 449, 61
———. 2006b, Nature, 442, 1008
———. 2007, ApJ, 654, L17
Cardelli, J. A., Clayton, G. C., & Mathis, J. S. 1989, ApJ, 345, 245
Cenko, S. B. 2006, GCN Circ. 5844, http://gcn.gsfc.nasa.gov/gcn/gcn3/5844.gcn3
Cenko, S. B., et al. 2006, ApJ, 652, 490

Chandra, P., & Frail, D. A. 2006, GCN Circ. 5843, http://gcn.gsfc.nasa.gov/gcn/gcn3/5843.gcn3
Cheng, L. X., Ma, Y. Q., Cheng, K. S., Lu, T., & Zhou, Y. Y. 1995, A&A, 300, 746
Chester, M., Page, M., Roming, P., Marshall, F., Boyd, P., Angelini, L., Greiner, J., & Gehrels, N. 2005, GCN Circ. 3838, http://gcn.gsfc.nasa.gov/gcn/gcn3/3838.gcn3
Chevalier, R. A., & Li, Z.-Y. 2000, ApJ, 536, 195
Cobb, B. E. 2006, GCN Circ. 5878, http://gcn.gsfc.nasa.gov/gcn/gcn3/5878.gcn3
Cummings, J., et al. 2005, GCN Circ. 3835, http://gcn.gsfc.nasa.gov/gcn/gcn3/3835.gcn3
den Herder, J. W., et al. 2001, A&A, 365, L7
Dermer, C. D. 2004, ApJ, 614, 284
de Ugarte Postigo, A., et al. 2007, A&A, 462, L57
Dickey, J. M., & Lockman, F. J. 1990, ARA&A, 28, 215
Diplas, A., & Savage, B. D. 1994, ApJ, 427, 274
Efimov, Yu., Rumyantsev, V., & Pozanenko, A. 2006a, GCN Circ. 5850, http://gcn.gsfc.nasa.gov/gcn/gcn3/5850.gcn3
———. 2006b, GCN Circ. 5870, http://gcn.gsfc.nasa.gov/gcn/gcn3/5870.gcn3
Fan, Y. Z., & Wei, D. M. 2005, MNRAS, 364, L42
Fenimore, E. E., in't Zand, J. J. M., Norris, J. P., Bonnell, J. T., & Nemiroff, R. J. 1995, ApJ, 448, L101
Fenimore, E. E., & Ramirez-Ruiz, E. 1999, ApJ, submitted (astro-ph/9909299)
Ford, L. A., et al. 1995, ApJ, 439, 307
Frail, D. A., et al. 2001, ApJ, 562, L55
Fukugita, M., Shimasaku, K., & Ichikawa, T. 1995, PASP, 107, 945
Galama, T. J., & Wijers, R. A. M. J. 2001, ApJ, 549, L209
Gehrels, N., Page, K., Barthelmy, S., Burrows, D. N., Marshall, F., Roming, R., Sakamoto, T., & Sato, G. 2006a, GCN Circ. 5839, http://gcn.gsfc.nasa.gov/gcn/gcn3/5839.gcn3
Gehrels, N., et al. 2004, ApJ, 611, 1005
———. 2006b, Nature, 444, 1044
Ghirlanda, G., Ghisellini, G., & Lazzati, D. 2004, ApJ, 616, 331
Ghisellini, G., Celotti, A., & Lazzati, D. 2000, MNRAS, 313, L1
Goad, M. R., et al. 2007, A&A, in press (astro-ph/0612661)
Golenetskii, S., Aptekar, R., Mazets, E., Pal'shin, V., Frederiks, D., & Cline, T. 2006, GCN Circ. 5837, http://gcn.gsfc.nasa.gov/gcn/gcn3/5837.gcn3
Golenetskii, S. V., Mazets, E. P., Aptekar, R. L., & Ilinskii, V. N. 1983, Nature, 306, 451
Guetta, D., et al. 2007, A&A, 461, 95
Guidorzi, C., et al. 2005, ApJ, 630, L121
Hakkila, J., & Giblin, T. W. 2004, ApJ, 610, 361
Halpern, J. P., & Armstrong, E. 2006a, GCN Circ. 5851, http://gcn.gsfc.nasa.gov/gcn/gcn3/5851.gcn3
———. 2006b, GCN Circ. 5853, http://gcn.gsfc.nasa.gov/gcn/gcn3/5853.gcn3
Halpern, J. P., Mirabal, N., & Armstrong, E. 2006a, GCN Circ. 5840, http://gcn.gsfc.nasa.gov/gcn/gcn3/5840.gcn3
———. 2006b, GCN Circ. 5847, http://gcn.gsfc.nasa.gov/gcn/gcn3/5847.gcn3
Hill, J. E., et al. 2004, Proc. SPIE, 5165, 217
———. 2006, ApJ, 639, 303
in't Zand, J. J. M., & Fenimore, E. E. 1996, ApJ, 464, 622
Jansen, F., et al. 2001, A&A, 365, L1
Klotz, A., Gendre, B., Stratta, G., Atteia, J. L., Boër, M., Malacrino, F., Damerdji, Y., & Behrend, R. 2006, A&A, 451, L39
Koornneef, J. 1982, A&A, 107, 247
Kulkarni, S. R., et al. 1999, Nature, 398, 389
Kumar, P., & Panaitescu, A. 2000, ApJ, 541, L51
Lazzati, D. 2005, MNRAS, 357, 722
Lazzati, D., Morsony, B. J., & Begelman, M. C. 2007, Philos. Trans. R. Soc. London A, 365, 1141
Liang, E. W., et al. 2006, ApJ, 646, 351
Link, B., Epstein, R. I., & Priedhorsky, W. C. 1993, ApJ, 408, L81
Lloyd, N. M., & Petrosian, V. 2000, ApJ, 543, 722
Madau, P. 1995, ApJ, 441, 18
Madau, P., Ferguson, H. C., Dickinson, M. E., Giavalisco, M., Steidel, C. C., & Fruchter, A. 1996, MNRAS, 283, 1388
Malesani, D., et al. 2006, GCN Circ. 5877, http://gcn.gsfc.nasa.gov/gcn/gcn3/5877.gcn3
Marshall, F. E. 2006, GCN Circ. 5899, http://gcn.gsfc.nasa.gov/gcn/gcn3/5899.gcn3
Marshall, F. E., Holland, S. T., & Page, K. L. 2006, GCN Circ. 5833, http://gcn.gsfc.nasa.gov/gcn/gcn3/5833.gcn3
Medvedev, M. V. 2000, ApJ, 540, 704
Melandri, A., et al. 2006, GCN Circ. 5827, http://gcn.gsfc.nasa.gov/gcn/gcn3/5827.gcn3
Mészáros, P., & Rees, M. J. 1999, MNRAS, 306, L39
Mészáros, P., Rees, M. J., & Papathanassiou, H. 1994, ApJ, 432, 181
Miyazaki, A., & Tsuboi, M. 1999, Adv. Space Res., 23, 973
Mundell, C. G., et al. 2007, ApJ, 660, 489
Nakamura, T. 2000, ApJ, 534, L159
Norris, J. P. 2002, ApJ, 579, 386
Norris, J. P., & Bonnell, J. T. 2006, ApJ, 643, 266
Norris, J. P., Marani, G. F., & Bonnell, J. T. 2000, ApJ, 534, 248
Norris, J. P., Nemiroff, R. J., Bonnell, J. T., Scargle, J. D., Kouveliotou, C., Paciesas, W. S., Meegan, C. A., & Fishman, G. J. 1996, ApJ, 459, 393
Nousek, J. A., et al. 2006, ApJ, 642, 389
Oates, S. R., et al. 2007, MNRAS, submitted
O'Brien, P. T., et al. 2006, ApJ, 647, 1213
Paciesas, W. S., et al. 1999, ApJS, 122, 465
Page, K. L., Beardmore, A. P., Goad, M. R., Kennea, J. A., Burrows, D. N., Marshall, F., & Smale, A. 2005a, GCN Circ. 3837, http://gcn.gsfc.nasa.gov/gcn/gcn3/3837.gcn3
Page, K. L., Starling, R. L. C., Osborne, J. P., Troja, E., & Morris, D. 2006a, GCN Circ. 5832, http://gcn.gsfc.nasa.gov/gcn/gcn3/5832.gcn3
Page, M., et al. 2005b, GCN Circ. 3830, http://gcn.gsfc.nasa.gov/gcn/gcn3/3830.gcn3
———. 2006b, GCN Circ. 5823, http://gcn.gsfc.nasa.gov/gcn/gcn3/5823.gcn3
Panaitescu, A., & Kumar, P. 2000, ApJ, 543, 66
———. 2004, MNRAS, 350, 213
———. 2007, MNRAS, 376, 1065
Panaitescu, A., & Mészáros, P. 1999, ApJ, 526, 707
Panaitescu, A., Mészáros, P., Burrows, D., Nousek, J., Gehrels, N., O'Brien, P., & Willingale, R. 2006a, MNRAS, 369, 2059
Panaitescu, A., Mészáros, P., Gehrels, N., Burrows, D., & Nousek, J. 2006b, MNRAS, 366, 1357
Pe'er, A., Mészáros, P., & Rees, M. J. 2005, ApJ, 635, 476
Pe'er, A., & Zhang, B. 2006, ApJ, 653, 454
Pei, Y. C. 1992, ApJ, 395, 130
Perley, D. A., & Bloom, J. S. 2006, GCN Circ. 5825, http://gcn.gsfc.nasa.gov/gcn/gcn3/5825.gcn3
Pilla, R. P., & Loeb, A. 1998, ApJ, 494, L167
Piro, L., et al. 1998, A&A, 329, 906
Ramirez-Ruiz, E., Celotti, A., & Rees, M. J. 2002a, MNRAS, 337, 1349
Ramirez-Ruiz, E., MacFadyen, A. I., & Lazzati, D. 2002b, MNRAS, 331, 197
Rees, M. J., & Mészáros, P. 2005, ApJ, 628, 847
Romano, P., et al. 2006, A&A, 456, 917
Roming, P. W. A., et al. 2005, Space Sci. Rev., 120, 95
Sari, R., & Esin, A. A., 2001, ApJ, 548, 787
Sari, R., & Piran, T. 1999, ApJ, 520, 641
Sari, R., Piran, T., & Halpern, J. P. 1999, ApJ, 519, L17
Sari, R., Piran, T., & Narayan, R. 1998, ApJ, 497, L17
Schady, P., et al. 2006, MNRAS, submitted (astro-ph/0611081)
———. 2007, MNRAS, 377, 273
Schartel, N. 2006, GCN Circ. 5829, http://gcn.gsfc.nasa.gov/gcn/gcn3/5829.gcn3
Schlegel, D. J., Finkbeiner, D. P., & Davis, M. 1998, ApJ, 500, 525
Sonoda, E., Maeno, S., Hara, T., Matsumura, T., Tanaka, K., Tanaka, T., & Yamauchi, M. 2006, GCN Circ. 5830, http://gcn.gsfc.nasa.gov/gcn/gcn3/5830.gcn3
Starling, R. L. C., Wijers, R. A. M. J., Wiersema, K., Rol, E., Curran, P. A., Kouveliotou, C., van der Horst, A. J., & Heemskerk, M. H. M. 2007, ApJ, in press (astro-ph/0610899)
Strüder, L., et al. 2001, A&A, 365, L18
Tang, S. M., & Zhang, S. N. 2006, A&A, 456, 141
Torii, K. 2006, GCN Circ. 5845, http://gcn.gsfc.nasa.gov/gcn/gcn3/5845.gcn3
Turner, M. J. L., et al. 2001, A&A, 365, L27
Uemura, M., Arai, A., & Uehara, T. 2006, GCN Circ. 5828, http://gcn.gsfc.nasa.gov/gcn/gcn3/5828.gcn3
Umeda, H., Tominaga, N., Maeda, K., & Nomoto, K. 2005, ApJ, 633, L17
van der Horst, A. J., Wijers, R. A. M. J., & Rol, E. 2006a, GCN Circ. 5871, http://gcn.gsfc.nasa.gov/gcn/gcn3/5871.gcn3
———. 2006b, GCN Circ. 5874, http://gcn.gsfc.nasa.gov/gcn/gcn3/5874.gcn3
Vaughan, S., et al. 2006, ApJ, 638, 920
Vestrand, W. T., et al. 2005, Nature, 435, 178
———. 2006, Nature, 442, 172
Waxman, E., & Draine, B. T. 2000, ApJ, 537, 796
Waxman, E., & Mészáros, P. 2003, ApJ, 584, 390
Willingale, R., et al. 2007, ApJ, in press
Wilms, J., Allen, A., & McCray, R. 2000, ApJ, 542, 914
Wilson, T. L., Mauersberger, R., Gensheimer, P. D., Muders, D., & Bieging, J. H. 1999, ApJ, 525, 343
Yost, S. A., Schaefer, B. E., & Yuan, F. 2006, GCN Circ. 5824, http://gcn.gsfc.nasa.gov/gcn/gcn3/5824.gcn3
Zhang, B., Fan, Y. Z., Dyks, J., Kobayashi, S., Mészáros, P., Burrows, D. N., Nousek, J. A., & Gehrels, N. 2006, ApJ, 642, 354
Zhang, B., & Mészáros, P. 2002, ApJ, 581, 1236
———. 2004, Int. J. Mod. Phys. A, 19, 2385
Zhang, B.-B., Liang, E.-W., & Zhang, B. 2007, ApJ, in press (astro-ph/0612246)